RESEARCH ON HEAT TRANSFER CHARACTERISTICS OF FRACTAL-GENERATED TURBULENCE BASED ON LARGE EDDY SIMULATION

by

Chengdong DUAN, Yuncong JIANG, Nannan WU**, Qiwen XU, and Lijun WANG

School of Electrical and Power Engineering, China University of Mining and Technology, Xuzhou, Jiangsu, China

Original scientific paper
https://doi.org/10.2298/TSCI181122108D

Turbulence plays an important role in the fields of heat and mass transfer and enhanced chemical reaction. In order to explore the effect of grid-generated turbulence on flow heat transfer, in this paper, three different fractal grid structures with the same blocking ratio σ, effective mesh size M_{eff} *and thickness ratio* $t_r = t_{\max}/t_{\min}$ *(Case1: The grid cross-section is a triangle, Case2: the grid cross-section is an inverted triangle, Case3:the grid cross-section is square, Case4:no grid) and without the grid were simulated based on large eddy simulation. The aim of this simulation is to explain the evolution characteristics and heat transfer mechanism of turbulent flow field under the four cases. The results show that, in the same initial condition, Case 2 can generate the highest turbulence intensity and the feature of heat transfer on the cylindrical surface is more uniform. In Case 3, the boundary-layer in the flow field is separated earlier, and more vortices are excited to enhance the heat transfer than other cases in the boundary-layer region. The surface average Nusselt number is 1.3 times than that of Case 4.*

Key words: *fractal structure, grid turbulence, heat transfer, large eddy simulation*

Introduction

The flow under different turbulent state has greatly influenced the heat transfer characteristics. For example, turbulence intensity, pressure drop, homogeneous isotropic and other turbulence parameters will significantly affect the turbulent heat transfer. The effects of turbulent flows on the heat transfer from cylinders are of interest in different engineering applications [1]. It is common to use cylindrical geometry in actual engineering to exchange heat between fluid and wall, such as shell-and-tube heat exchangers, pressurized water reactors, water-to-air radiators, *etc.* [2]. In 1935, Taylor G. I. created irregular disturbances in the air-flow by placing a row or rows of regular grids in the wind tunnel. Irregular disturbances occurred when a uniform air-flow vertically passed through the grid. During the irregular disturbance moving to the downstream, due to no external interference, it has gradually evolved into homogeneous isotropic turbulence. Similar homogeneous isotropic turbulence has been extensively studied in wind tunnels or water tunnels, and direct numerical simulation (DNS) has been performed in the

* Corresponding author, e-mail: wucumt@163.com

periodic square computational domain by using the spectral method. Hurst *et al.* [3] used various multi-scale (fractal) grids to generate turbulence in wind tunnels, and found that complex multi-scale grid structures can greatly affect the behavior of turbulence and explored the fractal dimension $D_f \leq 2$, grid effective size M_{eff} and grid thickness ratio $t_r = t_{\max}/t_{\min}$ by experimental methods. These three factors greatly influence the mechanism of flow, isotropic, uniformity and attenuation characteristics of fractal-generated turbulence.

Melina [4] investigated the flow on the centerline of grid-generated turbulence for grids with different geometry: a fractal grid (FSG17), a single square grid (SSG), a regular grid (RG60). It is found that the turbulence intensity generated by the single grid structure is larger than the other two cases in the production region, which is due to the stronger vortex shedding effect, and the fractal grid suppresses the vortex shedding. Torrano [5] compared experimental measurement with RANS-Based numerical studies of the decay of grid-generated turbulence. The result showed the ability of RANS-based numerical simulations to capture the large scale properties generated by grid is within an acceptable accuracy. Hearst and Lavoie [6] designed a novel square-fractal-element grid in tunnel experiment to increase the downstream measurement range of fractal grid experiment. Their results demonstrate that the turbulence generated by the novel grid behaves in a manner similar to that observed in previous fractal studies near the grid, and the far downstream turbulence performance is similar to that produced by the regular grid. Panda *et al.* [7] compared grid generated turbulence with and without mean strain. They recommend optimal values of coefficients that should be used for experiment studies of grid generated turbulence. The previous conclusions provide theoretical bases and experimental bases for studying the influence of the turbulent parameters on the heat transfer effect [8, 9]. Smith *et al.* [10] developed a theoretical model by assuming that in the proximity of the front stagnation point Reynolds stress are proportional to the turbulence intensity, *Tu*, in the free-stream (flow approaching the cylinder) and to the distance from the wall. Their model, supported by experimental results, showed that the Frossling number at the front stagnation point was directly proportional to the turbulence parameter $Tu\,\text{Re}^{0.5}$, where Re is the Reynolds number based on the diameter, *D,* of the cylinder and on the mean streamwise velocity, *U*. Kestin *et al.* [11] and Lowery and Vachon [12] measured, respectively, the mass transfer and the heat transfer from a cylinder in a turbulent cross-flow generated by grids in a wind tunnel. Both studies correlated the values of $\text{Nu}_{\text{Fsp}}/\text{Re}^{0.5}$ with a second-degree polynomial function of $Tu\,\text{Re}^{0.5}$. In addition, several experiments show that the integral length scale, L_u, at the flow is also very important [13]. Van Der Hegge Zijnen [14] reported that when Reynolds number and *Tu* are the same, when $0 < L_u/D < 1.6$, Nusselt number increases with the L_u/D ratio; when $L_u/D > 1.6$, Nusselt number decreases with the L_u/D ratio, where *L* is defined as a length scale of turbulence. Recently, the vortex structure in the flow field has been extensively studied for enhanced heat transfer, and good heat transfer has been achieved by adding a vortex generator in the flow field [15-21].

With the improvement of computer technology, numerical simulation has become an important means of studying turbulence. There are three methods of numerical simulation commonly used: DNS, RANS, large eddy simulation (LES). The DNS can obtain the in-depth data of turbulent statistics including high-order moments near the wall, while it can only be used to solve very limited types of turbulent flows. The RANS can properly predict the complex flow of high Reynolds number at the most economic approach, but the result is time-averaged and does not reflect the instantaneous information of the flow field. Typical examples of such models are the *k*-*ε* or the *k*-*ω* models in their different forms. Recently, many Reynolds stress models have been developed by correcting the pressure-strain correlation of turbulence [22-25].

The LES directly predict the large-scale vortex motion, for only the smallest (subgrid scale) and more nearly isotropic vortices [26], sub-grid scale (SGS) model is adopted. Not only can the detailed flow field dynamic information be obtained, but also the calculation cost can be saved. Therefore, LES has been more and more widely used.

In view of the above analysis, in this paper, LES is used to study the turbulent flow generated by three different cross-section grids and the heat transfer of the constant temperature cylinder in the flow field. Three cross-sectional shapes are different for the turbulence generating device: triangle, an inverted triangle and the square. The blocking ratio is $\sigma = 0.28$, and the instantaneous and statistical properties such as velocity field, turbulence intensity, pressure drop, and Nusselt number are given to illustrate the mechanism of fluid motion and heat transfer under different perturbations, as well as the relationship between turbulence characteristics and heat transfer.

Numerical simulation method

Computing domain and meshing

The LES method is currently one of the effective tools for numerical study of turbulent flow and half way between the direct solution and RANS method. In the LES method, the scales that are below the mesh size are modelled by SGS, the scales that are higher than the mesh size are modelled directly by solving Navier-Stokes equation. The accuracy of LES results is high with the appropriate sub-grid mode. The computational cost of LES is lower than that of DNS. The simulation results could get the realer transient flow field, which helps to understand the nature of turbulent flow.

The problem, which was studied based on LES, is that the different flow fields generated by the fluid through the grid will arise different heat exchange effects on the cylinder. As shown in fig. 1, the specific simulation scheme is: In a $L_x \times L_y \times L_z$=1.2 m $\times$ 0.2 m $\times$ 0.2 m cuboid wind tunnel, in Case 1, Case 2, and Case 3, three types of grids with different shapes are placed at 0.1 m from the entrance, placing a constant temperature cylinder with a diameter of $D = 0.05$ m and a length of 0.2 m and temperature of 323 K at a distance of 0.5 m from the grid in all four cases. In order to eliminate the incomparability of the size factor, the calculation domain is dimensionless based on the diameter D of the heat exchange cylinder. The computational domain after dimensionless is $L_x \times L_y \times L_z = 24D \times 4D \times 4D$.

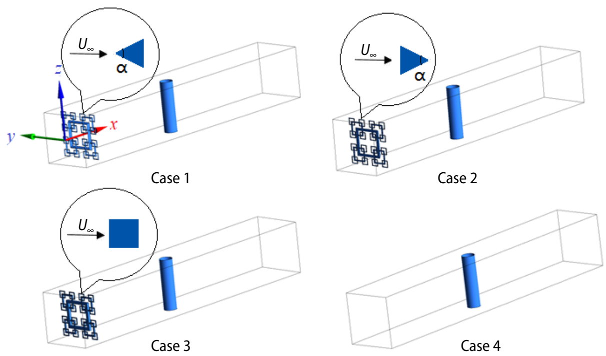

Figure1. Computational domain

These fractal grids are completely characterized by:
- the number of fractal iterations, here N=3;
- the number 4^j of square patterns at iteration j;
- the lengths $L_j = R_L^j L_0$ and lateral thickness $R_L = R_t = 0.5$, here L_0=0.5L_y, $t_0 = t_{\min}$=0.0025m
- the thickness ratio $t_r = t_{\max}/t_{\min}$, *i. e.* the ratio between the lateral thickness of the bars making the largest square and the lateral thickness of the smallest. Here t_r=4
- effective mesh size for multiscale grids $M_{eff} = 4T^2(1-\sigma)^{1/2}/L_{TG}$. Unlike regular grids, multiscale/fractal grids, and in particular the fractal grids considered here, do not have a well-de-

fined mesh size, This is the reason that Hurst *et al.* [3] introduced an effective mesh size for multiscale grids. L_{TG} is the total perimeter of the fractal grid on the x-y plane, in this paper $M_{eff} = 4.85t_{\min}$.
– Angle of the triangular prism grid α. In this paper, the evolution law of turbulent flow in triangular prism fractal grid is studied specially. Here $\alpha = 53°$.

Considering that the quality of the structural mesh at the intersection of the triangular prisms is difficult to guarantee, the unstructured grid is used in the entire computational domain of the Case 1 and 2. To ensure higher calculation accuracy, we set $y^+ = \Delta y \times u_\infty/\nu = 1$, thus, the first layer of mesh has a thickness of 0.056 mm. The y^+ is the dimensionless distance from the centroid of the first layer mesh to the wall. The Δy is the distance from the wall to the centroid of the first layer mesh. The MESH was used to generate tetrahedral unstructured mesh in Case 1 and 2. Curvature size function was chosen to control important extreme bending and mesh growth and distribution in adjacent areas of the surface. We set min size, max face size, max tex size to $2.0 \cdot 10^{-5}$ m, 0.002 m, 0.005 m, respectively. The total nodes are 1629407 and the total elements are 8917056.

Because the geometric models in Case 3 and Case 4 are simpler, the structured grid mesh with mesh numbers of 624 × 200 × 160 in the streamwise, wall-normal, and spanwise directions is used in Case 3 and Case 4.

Mathematical model

Control equation

The basic idea of LES is to separate large-scale eddies from small-scale eddies by filtering. To carry out the computation of the turbulent flow, continuity equation and Navier-Stokes equation are filtered:

$$\frac{\partial \overline{u_i}}{\partial x_i} = 0 \tag{1}$$

$$\frac{\partial \overline{u_i}}{\partial t} + \frac{\partial \overline{u_i}\,\overline{u_j}}{\partial x_j} = -\frac{1}{\rho}\frac{\partial \overline{p}}{\partial x_i}\left(\nu \frac{\partial \overline{u_i}}{\partial x_j} + \frac{\partial \overline{u_j}}{\partial x_i} - \tau_{ij}\right) \tag{2}$$

$$\tau_{ij} = \overline{u}_i\overline{u}_j + \overline{u}_i\overline{u}_j \tag{3}$$

where ρ is the fluid density, ν – the dynamic viscosity of the fluid, $\overline{u}_i$ – the filtered value of the velocity, $\overline{p}$ – the filtered value of the pressure, and τ_{ij} – the SGS, reflecting the influence of small-scale vortex on large-scale vortex. To close the filtered equations, the SGS stress is modelled using a viscous analogy:

$$\tau_{ij} = -2\mu_t \overline{s}_{ij} + \frac{1}{3}\delta_{ij}\tau_{ij} \tag{4}$$

$$\mu_t = (C_S\Delta)^2 \left|\overline{S_{ij}}\right| \tag{5}$$

$$\overline{s}_{ij} = \frac{1}{2}\left(\frac{\partial \overline{u}_i}{\partial \overline{x}_j} + \frac{\partial \overline{u}_j}{\partial \overline{x}_i}\right) \tag{6}$$

$$\mathit{\Delta} = (\Delta x \Delta y \Delta z)^{1/3} \tag{7}$$

where τ_{kk} is an isotropic part of the SGS, which is usually negligible in an incompressible flow, C_s – the Smagorinsky constant calculated from the inertial subrange of the energy spectrum given by the Kolmogorov's−5/3 law and it is chosen in a range from 0.10 to 0.30. The $\Delta \approx 0.86$ mm is the filter width, an indication of the characteristic length scale separates large and small-scale eddies from each other and can considered to be an average cell size. The μ_t is the SGS viscosity term. The $\overline{s}_{ij}$ is mean strain rate tensor.

Boundary conditions

The LES is a transient turbulence model, and its boundary conditions should be introduced into the time term.

- The initial Gauge pressure value is 0 Pa.
- The inlet velocity for all cases is set to $u_\infty = 5$ m/s which leads to a Reynolds number of $\mathrm{Re} = u_\infty l/\nu = 13611$, where l is hydraulic diameter of the cuboid wind tunnel. In Cases 1-3, no perturbations is added at the tunnel inlet, in Case 4, turbulence intensity $I = 0.16(\mathrm{Re}) \wedge (-1/8) = 6.4\%$ is added at the inlet.
- Outflow boundary conditions are used at the tunnel outlet boundary.
- No-slip condition and thermostatic wall $T = 283$ K are applied to wind tunnel walls and the grid. The cylinder is also set to be no-slip wall boundary and the temperature is 323 K.

In this study, LES simulations is carried out using a finite volume solver which employs a finite volume method for solving the incompressible Navier-Stokes equations within transient assumptions. The second order discrete format is used for the pressure term, and the bounded central differencing discrete format is used in the momentum equations. The numerical calculation method adopts the PISO algorithm, and the sub-grid model adopts the Smagorinsky-Lilly model. $C_s = 0.10$ is used for all simulations here [27].

Results and discussion

Simulation verification

In order to verify the correctness of the simulation results in this paper, we used the same simulation scheme to simulate the RG60 flow field studied in reference [4]. In fig. 2, we compared the streamwise mean velocity and turbulence intensity along the central line of the wind tunnel in the simulation and the wind tunnel test, which obtained a good agreement. The computation error is less than 25%. The $\overline{U}$ is definite as time-average streamwise velocity.

Flow characteristics

When the fluid flows around the cylinder, due to the frictional resistance between the fluid and the wall, boundary-layer is formed around the cylinder, and the flow in the boundary-layer region is laminar flow. There is no mutual mixing between the layers, so the heat transfer is mainly carried out by means of heat conduction. After the boundary-layer separation, heat is carried by the moving fluid due to the macroscopic mutual mixing, where the heat exchange is mainly convective heat transfer.

Analysis of velocity distribution

In this paper, by analyzing the contours and data of instantaneous streamwise velocity, the characteristic parameters and heat transfer effects of the turbulent field are obtained. Since the flow in the calculation domain has not been fully developed for the beginning of the flow, the data from 0-0.35 seconds is omitted. Only data from 0.35-0.55 seconds was selected for

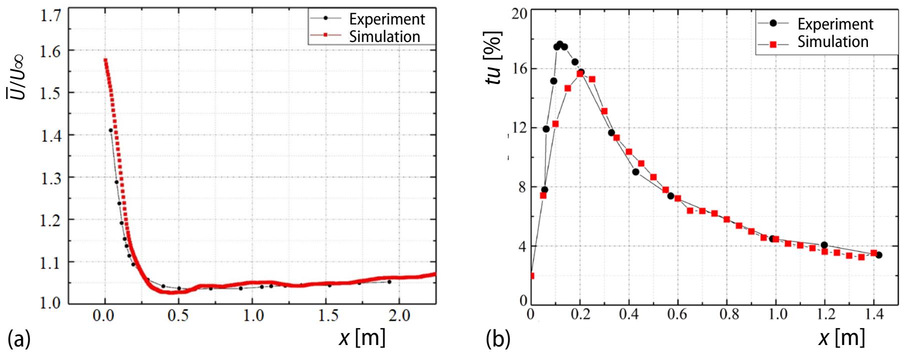

Figure 2. Mean velocity (a) and turbulence intensity (b) along the central line of the wind tunnel with distance downstream of the grid

analysis. All cases share the same Cartesian co-ordinate system with common origin, in which x is the streamwise direction starting just downstream of the grid, and y and z are the other two orthogonal directions. As a qualitative information, contours plots on the x-y plane ($y = 0$) as well as cross-stream planes situated on the $x/D = 2$, $x/D = 10$, $x/D = 12.5$ are provided. Quantitatively, different variables along the centerline of the wind tunnel and around the cylinder are displayed.

As shown in fig. 3, the contours plot of U is obtained at $t = 0.55$ seconds. U is definite as instantaneous streamwise velocity. When the flow passes through the grid, a low-speed zone is generated at the rear of the grid, and the vortex is gradually generated in the low-speed zone and alternately falls off along the streamwise direction. Comparing Case 1 with Case 2 and Case 3, the local low-speed area generated by the Case 2 is significantly larger than the other two cases. From the plane of $x/D = 2$, all cases with the grid have a more distinct geometrical imprints on the mean flow properties, the Case 3 is most obvious. In that, the shape of the grid do not change along the streamwise. The plane of $x/D = 12.5$ is placed on the surface behind the cylinder. A Karman vortex street occurs in the rear of the cylinder when the fluid flow around the

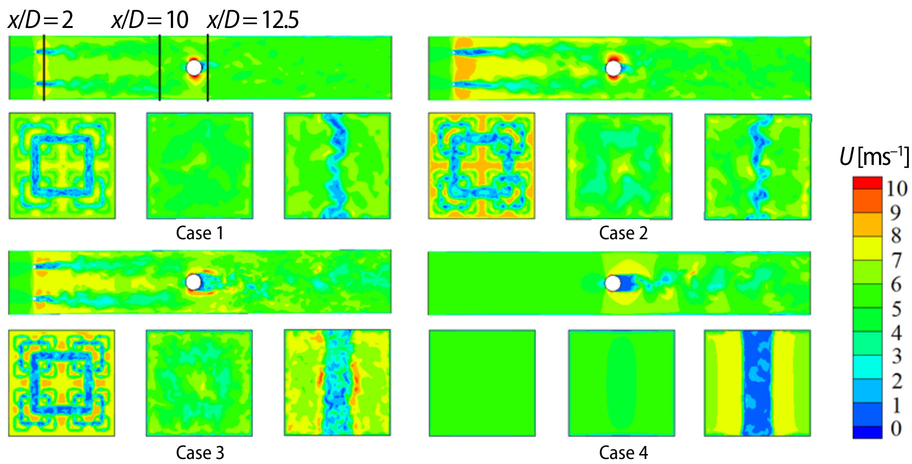

Figure 3. Instantaneous velocity contours plot extracted for the *x*-*z* plane (*y* = 0) and different cross-stream planes (x/D=2,10,12.5) at 0.5 seconds
(*for color image see journal web site*)

cylinder in Case 3 and Case 4. The reason is that the flow around the cylinder is less turbulent in both cases, and a strong disturbance occurs when disturbed.

Figure 4 illustrates the streamwise mean velocity profile along the centerline of the flow field. For Cases 1-3 the streamwise mean velocity increases distinctly in the interval $0 \leq x/D \leq 2$, owing to the blockage radios. For the Case 2, the mean velocity of is highest up to 8.3 m/s and the velocity attenuation is lowest in all the cases. In addition, for Case 3 and Case 4 vortices are generated in the rear of cylinder and shed off along the streamwise. The streamwise mean velocity near the rear of the cylinder sharply increase accompanied by a shock, until the speed returns to the inlet flow speed. Meanwhile, no obvious shocks occur in the Case 1 and the Case 2.

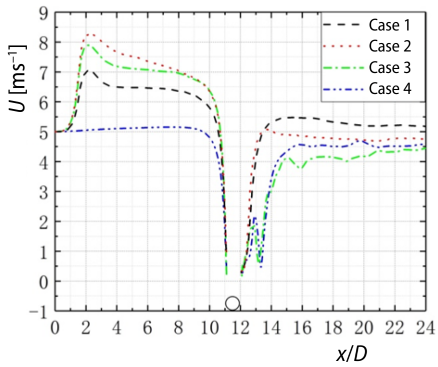

Figure 4. Mean velocity profile along the centerline

Turbulence intensity

Figure 5 shows the turbulence intensity, *Tu*, distribution along the centerline in four cases. Turbulence intensity is calculated by the following formula:

$$Tu = \frac{u'}{\overline{U}} \tag{8}$$

where u' is root mean square of instantaneous speed, $\overline{U}$ – the time-average streamwise velocity. From the formula, turbulence intensity is directly related to stochastic turbulent fluctuation. A higher turbulence intensity means greater stochastic turbulence fluctuations.

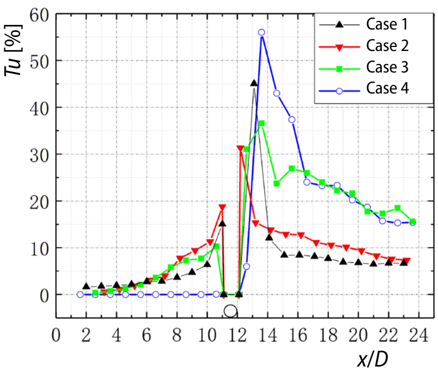

Figure 5. Turbulence intensity along the centerline

In figure, we find a increase of turbulence intensity with x/D in Cases 1-3 in front of the cylinder. In Case 3, the flow field produces the highest turbulence intensity up to 20%,owing to strong mixing. But, the turbulence intensity in Case 4 without grid is constant. At the back of cylinder, due to the cylinder disturbance, the flow becomes more turbulent. Case 4 produces the strongest turbulence intensity up to about 56%, which is about 48% in Case 1. Near the rear of the cylinder, for Case 3 and Case 4, the turbulence intensity shows a wavelike decrease, for Case 1 and Case 2, the turbulence intensity decrease progressively.

Analysis of pressure drop

In order to express the pressure distribution around the cylinder in the flow field, this paper introduces a dimensionless pressure drop formula, defined as: $f = 2(P - P_{\text{inlet}})/\rho u^2$, where p is the total pressure around the cylinder, ρ u – the density and average velocity at the inlet, and P_{inlet} – the total pressure of the inlet.

Figure 6 shows the boundary-layer separation when the air-flow around the cylinder. Figure 7 shows the velocity distribution around the cylinder. For all cases the mean velocity along the σ display parabola distribution, increasing firstly then decreasing and finally stabi-

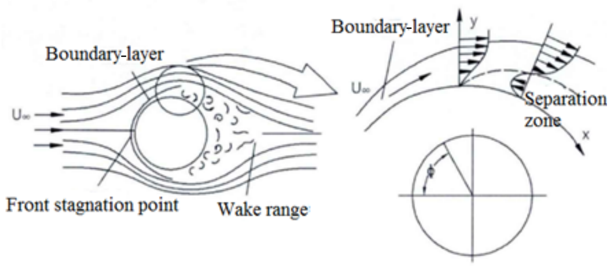

Figure 6. Schematic diagram of the formation of the boundary layer [28]

lizing. When the internal pressure gradient $\mathrm{d}p/\mathrm{d}x < 0$, the flow in the layer is accelerated, and the kinetic energy of the flow is increased. When $\mathrm{d}p/\mathrm{d}x > 0$, the pressure is opposite to the flow direction, and the flow in the boundary-layer is decelerated, and the kinetic energy is quickly exhausted. The shear stress in the boundary-layer near the cylinder surface is greater than that in the upstream fluid, and a reflow opposite the original flow direction occurs. This reflow separates the fluid in the boundary-layer and forms a boundary-layer separation. For Case 1 and Case 2 the boundary-layer separation occurs at $\phi \approx 100^{\circ}$, and for Case 3 and Case 4 the boundary-layer separation occurs at $\phi \approx 160^{\circ}$.

In fig. 8, we show the $0^{\circ} \leq \phi \leq 180^{\circ}$ pressure drop coefficient distribution around the cylinder in the flow field. We find that the Case 1 and Case 2 have a linear downward trend around the cylinder, for Case 1 the change of pressure drop coefficient is very small and nearly unchanged. For Case 3 and Case 4 the trend of pressure drop coefficient are nearly same. The pressure drop coefficient is the largest at $\phi = 0^{\circ}$, and the data decreases exponentially at $0^{\circ} \leq \phi \leq 80^{\circ}$. At $\phi = 80^{\circ}$, the pressure drop coefficient drops to the lowest point and reflow begins to appear, at which point $\mathrm{d}p/\mathrm{d}x = 0$. It rises between $80^{\circ} \leq \phi \leq 100^{\circ}$, then becomes stable. Meanwhile, the kinetic energy of the boundary-layer is exhausted and the boundary-layer begins to separate. However, the minimum pressure drop coefficient of Case 3 is about –4.5, which is lower than –3.5 for Case 4. Moreover, in $100^{\circ} \leq \phi \leq 180^{\circ}$, the data of Case 3 could be maintained at –2.5 and Case 4 at –3.3.

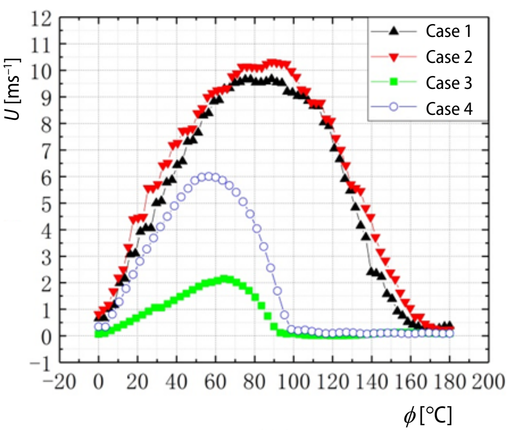

Figure 7. Velocity around the cylinder

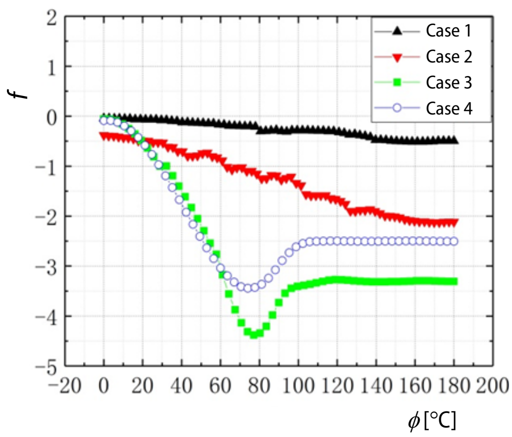

Figure 8. Pressure drop around the cylinder

Vortex structure

According to the incompressible Navier-Stokes equation, Jeong and Hussain [16] Sorted the eigenvalues of the combined tensor $\mathbf{D}^2 + \mathbf{\Omega}^2$ of the strain rate tensor, $\mathbf{D}$, and the vortex tensor, $\mathbf{\Omega}$, coming to the conclusion $\lambda_1 \geq \lambda_2 \geq \lambda_3$. The necessary and sufficient condition for the vortex core pressure reaching the minimum cross-section is $\lambda_2 \leq 0$, called the λ_2 criterion.

Figure 9 shows the vortex structure in four cases. In Case 1 and Case 2, the flow field only produces a more obvious vortex at the rear of the cylinder but less than that of Case 4. For Case 3 the flow field excites more vortices on the entire cylinder surface, and it is these vortexes that are close to the cylinder that enhance the heat transfer.

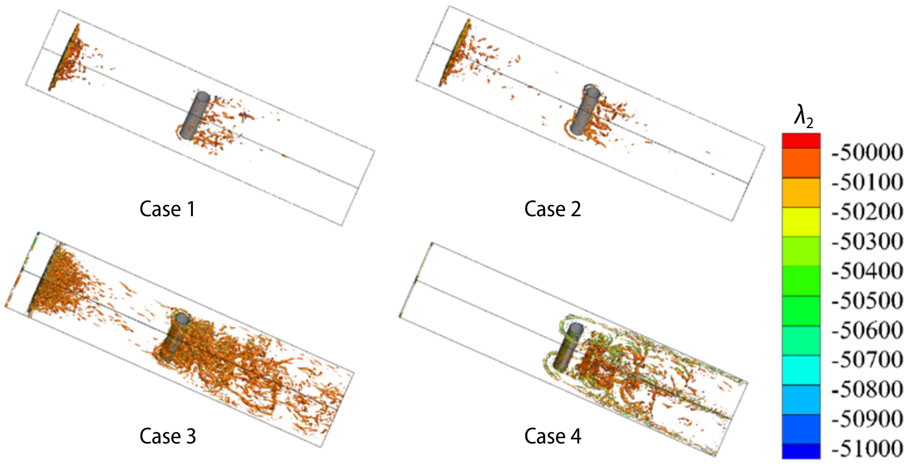

Figure 9. Vortex structure λ_2 between –5000 and –51000
(*for color image see journal web site*)

Heat transfer characteristics

Figure 10 shows the Nusselt number contour plots of the cylindrical surface in four cases, and the top view of the heating cylinder, the front view (facing the incoming flow direc-

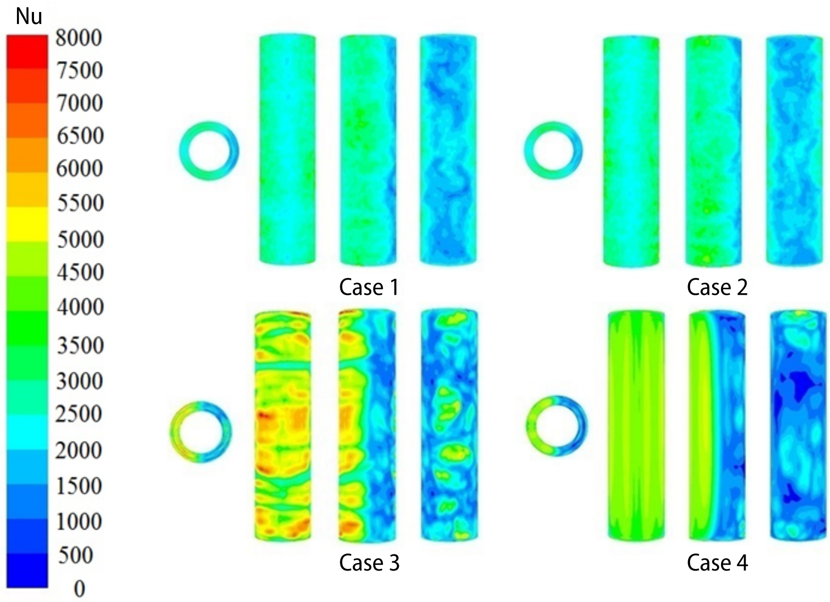

Figure 10. Surface Nusselt number of the cylinder the top view of the heating cylinder, the front view (facing the incoming flow direction), the side view, and the rear view (*for color image see journal web site*)

tion), the side view, and the rear view are, respectively, selected. Heat conduction is dominated in the boundary-layer while heat convection is dominant in the wake area. In addition, the heat conduction effect in the boundary-layer is stronger than the heat convection generated by the vortex shedding in the wake region. Therefore, the heat transfer effect of the cylindrical boundary-layer region is stronger than that of the wake area. The θ is boundary-layer separation angle, *i. e.* the angle between the x and the line between boundary-layer separation point and the center of a circle. For Case 1 and Case 2 $\theta \approx 135°$ is much larger than $\theta \approx 85°$ of Case 3 and Case 4. In addition, the distribution of Nusselt number under Case 1-3 is very uneven in boundary-layer region. Especially in the Case 3, the area with large Nusselt number (≥ 6000) exists in the boundary-layer region. This can be explained by the presence of generated disturbance, therefore, convective heat transfer occurs in the boundary-layer region.

Figure 11 illustrates that the contours plot of the temperature is obtained on the plane $z = 0$. The conclusion drawn from fig. 11 get a good match intuitively with the figs. 8-10.

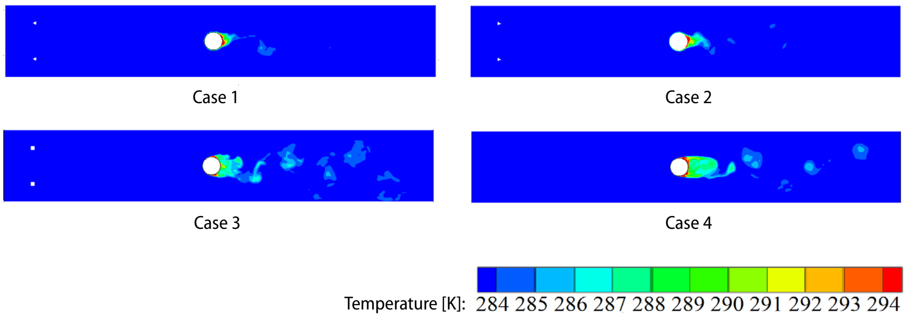

Figure 11. Temperature contours plot on the plane $z = 0$ at $t = 0.5$ seconds
(*for color image see journal web site*)

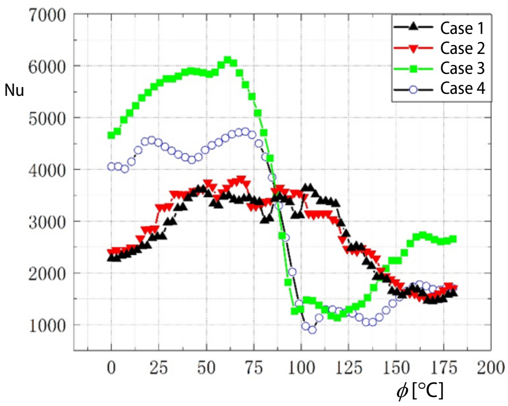

Figure 12. Nusselt number around the cylinder

Figure 12 shows the Nusselt number distribution of $0^\circ \leq \phi \leq 180^\circ$. Between $0^\circ \leq \phi \leq 78^\circ$, the maximum Nusselt number of Case 3 is about 6200, which is about 30% higher than that of Case 4, about 63% higher than Case 1 and Case 2. However, it drops sharply between $78^\circ \leq \phi \leq 105^\circ$, reaching a minimum value 1000, and gradually recovers from $105^\circ \leq \phi \leq 180^\circ$ and finally reaches to about 2600. It shows that the heat exchange effect for Case 3 is not uniform. In terms of surface average Nusselt, heat transfer effect of Case 3 is best in the four cases, which is up to 3870, tab. 1.

Table 1. Surface average Nusselt number

	Case 1	Case 2	Case 3	Case 4
Surface average Nusselt	2493	2666	3870	2852

The trend and value of the two distributions in Case 1 and Case 2 are approximately the same without a sharp rise and fall. The gap between the maximum and minimum values is about 2300, which is much smaller than 5000 in the Case 3 and 4000 in the Case 4.

It shows that in Case 1 and Case 2 the flow field can produce a more uniform heat transfer effect, and the surface average Nusselt number is 2493, 2666, respectively.

Conclusions

Based on LES, the flow evolution and heat transfer around a cylinder in four flow fields (triangle grid, inverted triangle grid, square grid, and no grid) are simulated. The flow characteristics and heat transfer characteristics of the four flow fields are analyzed, and the following conclusions are drawn as follows.

- In this paper, the flow fields under triangular grid, inverted triangle, square grid and no grid perturbation are compared. It is found that the local low-speed region generated by the inverted triangle grid is significantly larger than other two cases, thus the higher turbulence intensity is produced.
- Case 1 and Case 2 present a linear downward trend in the pressure drop coefficient around the cylinder, in Case 1 the change of pressure drop coefficient is very small and nearly unchanged.
- In Case 1 and Case 2, the flow field can produce a more uniform heat transfer effect, but the overall heat transfer effect is not as good as Case 4.
- In Case 3 the boundary-layer is separated earlier, and more vortices are excited to enhance the heat transfer effect in the boundary-layer region, moreover, in terms of the surface average Nusselt number, heat transfer effect is best, surface average Nusselt number up to 3870.

Acknowledgment

This work is supported by *the Fundamental Research Funds for the Central Universities*, 2017XKZD02, and a project funded by the priority academic program development of Jiangsu higher education institutions.

References

[1] Melina, G., Heat Transfer in Production and Decay Regions of Grid-Generated Turbulence, *Int. J. Heat Mass Transfer, 109* (2017), 2, pp. 537-554
[2] Hewitt, G. F., *Heat Exchanger Design Handbook*, Begell House, New York, USA, 2008
[3] Hurst, D., *et al.*, Scalings and Decay of Fractal-Generated Turbulence, *Phys. Fluids., 19* (2007), ID 035103
[4] Melina, G., *et al.*, Vortex Shedding Effects in Grid-Generated Turbulence, *Phys. Rev. Fluids., 1* (2016), 4, ID 044402
[5] Torrano, M. T., *et al.*, Comparison of Experimental and Rans-Based Numerical Studies of the Decay of Grid-Generated Turbulence, *Journal of Fluids Engineering., 137* (2015), 6, ID 061203
[6] Hearst, R. J., Lavoie, P., Decay of Turbulence Generated by A Square-Fractal Element Grid, *Journal of Fluid Mechanics., 741* (2014), 2, pp. 567-584
[7] Panda, J., *et al.*, Experimental and Numerical Analysis of Grid Generated Turbulence with and without Mean Strain, *Experimental Thermal and Fluid Science., 98* (2018), 11, pp. 594-603
[8] Risberg, D., *et al.*, Computational Fluid Dynamics Simulation of Indoor Climate in Low Energy Buildings Computational Set Up, *Thermal Science, 21* (2017), 5, pp. 1985-1998
[9] Alammar, K, N., Turbulent Flow and Heat Transfer Characteristics in U-Tubes: A Simulation Study, *Thermal Science, 13* (2009), 4, pp. 175-181
[10] Smith, M. C., *et al.*, Effects of Turbulence on Laminar Skin Friction and Heat Transfer, *Phys. Fluids., 9* (1966), 12, pp. 2337-2344
[11] Kestin, J., *et al.*, The Influence of Turbulence on Mass Transfer from Cylinders, *J. Heat Transfer., 93* (1971), 4, pp. 321-327

[12] Lowery., G. W., Vachon, R. I., The Effect of Turbulence on Heat Transfer from Heated Cylinders, *Int. J. Heat Mass Transfer., 18* (1975), 6, pp. 1229-1242
[13] Sak, C., *et al*., The Role of Turbulence Length Scale and Turbulence Intensity on Forced Convection from a Heated Horizontal Circular Cylinder, *Exp. Therm. Fluid Sci*., *31* (2007), 4, pp. 279-289
[14] Van Der Hegge Zijnen, B. G., Heat Transfer from Horizontal Cylinders to a Turbulent Air Flow, *Appl. Sci. Res., 7* (1958), 2-3, pp. 205-223
[15] Tian, L. T., *et al*., A Comparative Study on the Air-Side Performance of Wavy Fin-And-Tube Heat Exchanger with Punched Delta Winglets in Staggered and In-Line Arrangements, *International Journal of Thermal Sciences, 48* (2009), 9, pp. 1765-1776
[16] Jeong, J., Hussain, F., On the Identification of a Vortex, *Journal of Fluid Mechanics, 285* (1995), Feb., pp. 69-94
[17] Fiebig, M., *et al*., Wing-Type Vortex Generators for Fin-Tube Heat Exchangers, *Experimental Thermal and Fluid Science, 7* (1993), 4, pp. 287-295
[18] Biswas, G., *et al*., Heat Transfer Enhancement in Fin-Tube Heat Exchangers by Winglet Type Vortex Generators, *International Journal of Heat and Mass Transfer, 37* (1994), 2 pp. 283-291
[19] Jacobi, A. M., *et al*., Heat Transfer Surface Enhancement, Through the Use of Longitudinal Vortices – A Review of Recent Progress, *Experimental Thermal and Fluid Science*, *11* (1995), 3, pp. 295-309
[20] Gentry, M. C., *et al*., Heat Transfer Enhancement by Delta Wing Vortex Generators on a Flat Plate: Vortex Interactions with the Boundary Layer, *Experimental Thermal and Fluid Science*, *14* (1997), 3, pp. 231-242
[21] Mushatet, K. S., Simulation of Turbulent Flow and Heat Transfer over a Backward –Facing Step with Ribs Turbulators, *Thermal Science, 15* (2011), 1, pp. 245-255
[22] Panda, J. P., *et al*., An Improved Model Including Length Scale Anisotropy for the Pressure Strain Correlation of Turbulence, *ASME Journal of Fluids Engineering, 139* (2017), 1, ID.044503
[23] Mishra, A., Girimaji, S., Toward Approximating Non-Local Dynamics in Single-Point Pressure-Strain Correlation Closures, *Journal of Fluid Mechanics, 811* (2017), 25, pp. 168-188
[24] Panda, J. P., Warrior, H. V., A Representation Theory-Based Model for the Rapid Pressure Strain Correlation of Turbulence., *Journal of Fluids Engineering, 140* (2018), 8, ID.081101
[25] Mishra., A. A., Girimaji, S. S., Pressure–Strain Correlation Modeling: Towards Achieving Consistency with Rapid Distortion Theory, *Flow, Turbulence and Combustion, 85* (2010), 3-4, pp. 593-619
[26] Tao., W. Q., *Numerical Heat Transfer*, Xi'an Jiaotong University, Xi'an., China, 2001
[27] Zou L., *et al*., Large-Eddy Simulation of Flow Around Cylinder Arrays at a Subcritical Reynolds Number, *Journal of Hydrodynamics, 20* (2008), 4, pp. 403-413
[28] Guo, C. W., *et al*., *Engineering Fluid Mechanics*, Jiang Su., Nanjing, China, 2010

Paper submitted: November 22, 2018
Paper revised: March 6, 2019
Paper accepted: March 20, 2019